# RASE: A Real-Time Automatic Search Engine for Anomalous Seismic Electric Signals in Geoelectric Data

Jiyan Xue, Sihong Wu, Qinghua Huang, Li Zhao, Nicholas V. Sarlis, and Panayiotis A. Varotsos

*Abstract*— The geoelectric data contain important anomalous information for short-term earthquake prediction. Timely and accurate identification of seismic electric anomalies is important for disaster prevention. However, identifying anomalies is challenging due to the huge volumes of data and noise disturbance. In this study, we develop a real-time automatic search engine (RASE) that incorporates an unsupervised convolutional denoising network (UCN) module and a supervised LSTM prediction network (SLN) module to automatically search for important anomalous signals in real time. Experiments demonstrate that the RASE provides excellent detection accuracy and efficiency for synthetic and field data, which takes only dozens of seconds for a common personal computer (PC) to provide accurate detection results for data collected over a 24-h period. The RASE has excellent flexibility and developability, as its internal modules can be adapted by more suitable technologies for better performance in various application scenarios. The comparison of multiple module combinations shows that the RASE configured with UCN and SLN has the highest detection accuracy. Our proposed search engine can reduce the human labor required for complex and repetitive detection work and fully realize the potential of geoelectric field observation in earthquake monitoring and disaster prevention.

*Index Terms*— Deep learning, multimodule integration, seismic electric anomaly detection, seismo-electromagnetism.

## I. INTRODUCTION

CONTINUOUS observation of various geophysical signals is of great importance for earthquake monitoring and disaster prevention [1]. Many pre-earthquake geophysical anomalies have been reported, including seismicity [2], [3], [4], [5], [6], [7], as well as geoelectric [8], [9], [10], [11] and geomagnetic [12], [13], [14] fields. The geoelectric field data are sensitive to microscopic changes in the seismogenic zone, and existing statistical evidence has shown that certain geoelectric field anomaly, the so-called seismic electric signal (SES), correlates well with seismicity before impending earthquakes [4], [15]. Therefore, geoelectric field monitoring networks are widely deployed in seismically active areas to monitor precursor SESs [16]. Although the physical mechanism of anomalous SES generation is still controversial [17], [18], [19], [20], [21], [22], timely and accurate extraction of SESs from observations is necessary for monitoring the seismogenic processes so that geoelectric observation may be employed in disaster mitigation [1], [10].

Technicians generally distinguish abnormal SESs from the normal geoelectric field by waveform characteristic, time–frequency analysis, and natural time analysis [4], [23], [24], [25], [26], [27]. However, due to the wide distribution of geoelectric observation networks and the high sampling frequency, manual analysis of massive datasets is extremely tedious and time-consuming. Moreover, the presence of noise also makes it difficult to fully explore the embedded effective SESs, resulting in the loss of valuable information [28], [29]. Therefore, it is crucial to develop automatic and effective anomaly search techniques to reduce the tedious and repetitive manual labor and improve the timeliness and utilization of data.

Data-driven deep learning-based algorithms can extract more generalized high-level features in the data with powerful characterization capability [30]. In addition, a well-trained network can be directly applied to newly acquired data to meet the real-time requirement of anomaly detection [31]. Therefore, deep learning has been used for anomaly detection in many different disciplines, including medicine, transportation, computer network, aerospace, and many other fields with excellent performance [32], [33], [34], [35], [36], [37]. However, geoelectric field data are more susceptible to noise pollution generated by multiple unknown sources. So far, to our knowledge, only one automatic anomaly detection algorithm based on deep learning has been proposed by Kanarachos et al. [38], which combines wavelet and Hilbert transform with a fully connected network. However, it is difficult to replace the wavelet denoising in their algorithm by more advanced methods, and the input of their fully connected network is restricted to be multilevel decomposed data with simple features, which not only affects the configurability and scalability but also limits the detection performance of this algorithm.

Considering that the geoelectric field data are typical time series with obvious periodic characteristics [39], we adopt the long short-term memory (LSTM) network in the geo-electric field anomaly detection, which uses gate functions and tuple states to analyze the temporal information in the input data [40], [41] and is particularly effective in time series analysis [28], [29], [42], [43].

The irregular random noise in the raw geoelectric field data can seriously impede the detection of hidden SESs. In recent decades, various random noise distribution theories and denoising methods have been developed and applied in practice. These include signal decomposition that uses empir-ical modal decomposition (EMD) and principal component analysis [44], [45], [46]; sparse transform based on wavelet transformation [47]; and rank reduction by singular spectrum analysis (SSA) [48], [49]. However, most conventional denois-ing algorithms rely on careful tuning of empirical parameters to achieve satisfactory performance and lack sufficient flexi-bility to ensure accuracy in practical applications. Moreover, the efficiency of searching for anomalous SESs is consid-erably limited. Recently, deep learning-based unsupervised algorithms have shown great promise for suppressing random noise in seismic signals, which can quickly yield results with higher signal-to-noise ratios (SNRs) and fidelities without elaborate parameter tuning [50], [51], [52].

In this study, we propose a real-time automatic search engine (RASE) that incorporates an unsupervised convolu-tional denoising network (UCN) module and a supervised LSTM prediction network (SLN) module. We demonstrate the remarkable detection accuracy and efficiency of the RASE by both synthetic and field data using the receiver operating characteristic (ROC) analysis [53], [54] (see the Appendix for details). In addition, the RASE has excellent developa-bility, with internal modules easily replaced or combined to achieve the best performance according to diverse require-ments. A comparison of multiple module combinations shows that the RASE configured with UCN and SLN has the highest detection accuracy. Our proposed RASE can be applied to SES detection tasks and provide real-time and accurate search results from massive geoelectric observation data.

## II. DATA

We examine the effectiveness of the RASE using both synthetic data with artificial anomalous SESs and field data with manually detected real SESs. In the former case, we gen-erate synthetic data by randomly embedding simulated SESs into anomaly-free background geoelectric data. For the back-ground data, we collect a 60-d anomaly-free record starting from 1 January 1999 with a high SNR and a default sam-pling frequency of 0.1 Hz from station Niijima deployed by Rikagaku Kenkyusho (RIKEN) on an uninhabited island in the Izu Islands, Japan [39]. We add Gaussian and impulsive noises to the background data to simulate a strong noise environment and then divide the data into training, validation, and test sets by the ratio of 9:0.5:0.5 along the time axis. Based on the accumulated observations so far, anomalous SESs are approximately characterized by rectangular-shaped
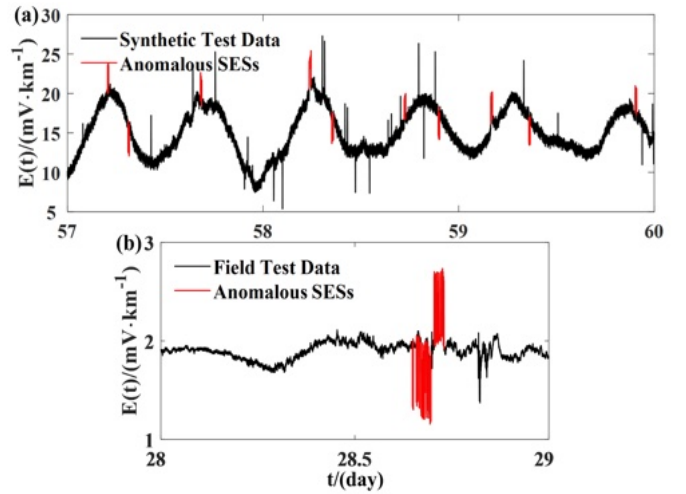


Fig. 1. Synthetic and field test data. (a) Artificial embedded anomalous SESs contained in synthetic test data shown by red lines. (b) Real anomalous SESs between 15:34 and 17:31 on 17 March 2001 (Day 29 in the selected duration) recorded at station VOL determined by experts. The real anomalous SESs consist of multiple approximately rectangular-shaped signals lasting a few minutes shown by red lines.

waveforms in the time domain, with durations ranging from a few minutes to several hours and amplitudes usually on the order of a few millivolts per kilometer above the background value [10], [15], [23], [29], [55]. Therefore, we randomly embed ten anomalous SESs with amplitudes of about 3 mV/km and durations of about 10 min into the test set [see Fig. 1(a)]. Binary labels (see the Appendix) are used to mark the anoma-lous SESs for quantitative evaluation.

The field data with real anomalous SESs are collected from the Volos (VOL) station deployed in an SES sensitive area of Volos in Greece with the default sampling rate of 0.1 Hz [56]. On 17 March 2001, station VOL recorded a strong anomalous disturbance for about 2 h, consisting of multiple near-rectangular-shaped signals [see Fig. 1(b)]. This anomaly was meticulously analyzed and determined as the SESs of the 26 July 2001 Aegean Sea M6.5 earthquake [56]. We demonstrate the RASE's performance using the 29-d record from 19 February to 17 March 2001. The data on 17 March are used as the test set, and the previous 28-d data are divided into training and validation sets by the ratio of 9:1.

## III. METHOD

### A. Structure of RASE

The entire data flow of the RASE is shown in Fig. 2(a). The RASE is composed of two critical modules [see Fig. 2(b) and (c)], with the overall aim of searching for anomalous SESs in the massive input observational data. The geoelectric field data are often contaminated with strong irregular noises that limit the ability of SLN to learn the hidden features in the data and interfere with the extraction of useful SESs. Therefore, the RASE employs a UCN module to suppress the noises and improve the signal quality. Subse-quently, an SLN is trained to learn the target-relevant features of the UCN-denoised geoelectric field data to iteratively pre-dict the data for the next sampling point. For data without
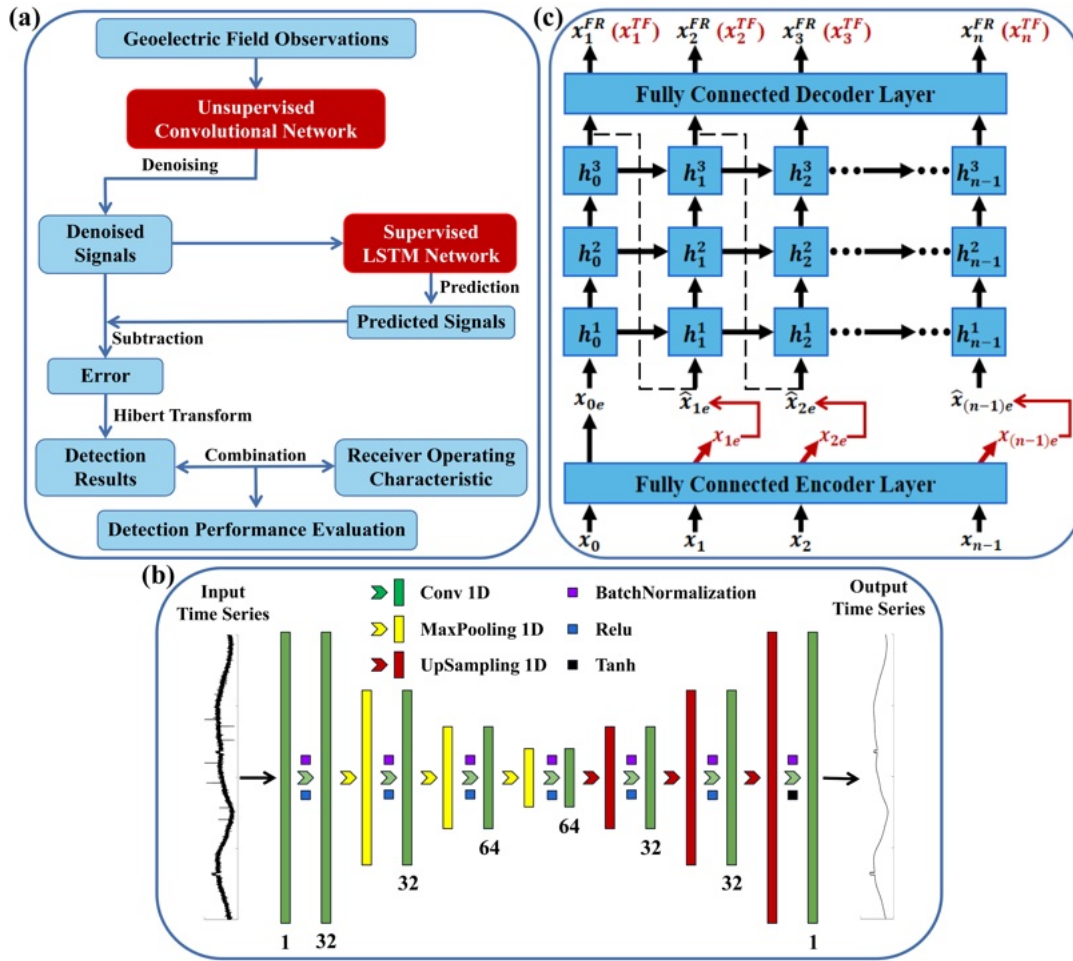
Fig. 2.    Framework of the RASE. (a) Internal flowchart and main functional modules. Modules with red backgrounds indicate parts that must be trained prior to application for each station. (b) UCN. The numbers of convolution kernel channels are given below the convolution layers. (c) SLN. The black and red texts indicate the input and output of the network in FR and TF training modes, respectively.

anomalous SESs, the well-trained SLN can provide accurate predictions with small errors between the predicted results and the denoised data. However, for data with anomalous SESs, the errors between the SLN-predicted results and the denoised data can be particularly large during the periods of SES occurrences. The RASE then uses the Hilbert transform to calculate the error envelopes (detection results) and determine the periods of anomalous SES occurrences. The amplitudes of the error envelopes represent the probability scores of the anomalies. A larger score indicates a higher probability of SES occurrence. A specific threshold value $S_T$ needs to be determined as the criterion for the occurrence of SES. Data in the period in which the probability score exceeds the specified threshold are considered to be abnormal SESs or normal otherwise. Furthermore, to quantitatively evaluate the anomaly detection performance of the RASE, we invoke the ROC analysis based on the manually labeled results. The area under the ROC curve is used to investigate the effect of threshold selection on detection accuracy.

### B. UCN Module

The UCN module [see Fig. 2(b)] can suppress irregular random noises in the raw data and improve the quality of

the training data for the subsequent SLN module and is thus helpful for the SLN to effectively extract the hidden features. The UCN automatically discards irregular noises by their random and unpredictable characteristics and reconstructs the regular and learnable features of the signal. Besides, the UCN can perform the denoising task without label constraints [57].

The whole network adopts an encoder–decoder structure [58] with convolutional, maximum pooling, and upsampling layers to compress and reconstruct the data. Batch normalization is introduced between adjacent network layers to avoid vanishing gradients and internal covariance shifts [59]. In the training phase, the UCN's input and output are the same noisy data, typical of unsupervised training. The loss function $L_{\text{UCN}}$ is the root-mean-square error (RMSE) between the input $\boldsymbol{x}^I$ and output data $\boldsymbol{x}^O$

$$L_{\text{UCN}}(\boldsymbol{W}_{\text{UCN}}, \boldsymbol{b}_{\text{UCN}}) = \sqrt{\frac{1}{m}\left[\sum_{i=1}^{m}\left(x_i^I - x_i^O\right)^2\right]} \quad (1)$$

where $\boldsymbol{W}_{\text{UCN}}$ and $\boldsymbol{b}_{\text{UCN}}$ represent the weighting matrices and bias vectors in the UCN, respectively, $x_i^I$ and $x_i^O$ are the elements of the input $\boldsymbol{x}^I$ and output data $\boldsymbol{x}^O$, respectively, and

$m$ is the number of sampling points in the input data ($m = 8640$, for daily data).

### C. SLN Module

The SLN [see Fig. 2(c)] consists of a fully connected encoding layer, a three-layer stacked LSTM network, and a fully connected decoding layer. It predicts the output data at the $n$th time sample based on the first $n-1$ samples in the input data and recursively predicts backward. The loss function of the SLN training consists of three components.

In the free-running (FR) mode [60], [61], the input data are encoded by the fully connected layer. The encoded data at the first sample point $x_{0e}$ are input to the stacked LSTM network to predict the data at the next sample point $\hat{x}_{1e}$ and then continue recursively backward $[\hat{x}_{2e}, \ldots, \hat{x}_{(n-1)e}]$. Finally, the fully connected decoding layer outputs the prediction results $[x_1^{FR}, x_2^{FR}, \ldots, x_n^{FR}]$. The first loss function $L_{SLN-FR}$ is the RMSE between the SLN-predicted results and the labels in the FR mode

$$L_{SLN-FR}(\boldsymbol{W}_{SLN}, \boldsymbol{b}_{SLN}) = \sqrt{\frac{1}{n}\left[\sum_{i=1}^{n}\left(x_i^{FR} - x_i\right)^2\right]} \quad (2)$$

where $\boldsymbol{W}_{SLN}$ and $\boldsymbol{b}_{SLN}$ represent the weighting matrices and bias vectors in the SLN, respectively, and $n$ is the number of sampling points ($n = 100$).

Since there are cumulative prediction errors in the FR mode, which impedes the loss function from stable convergence, we add a second loss function. In the teacher forcing (TF) model [61], we use the encoded data $[x_{1e}, x_{2e}, \ldots, x_{(n-1)e}]$ instead of the output data from the stacked LSTM layers $[\hat{x}_{1e}, \hat{x}_{2e}, \ldots, \hat{x}_{(n-1)e}]$ for subsequent prediction and decode it to get the prediction result $[x_1^{TF}, x_2^{TF}, \ldots, x_n^{TF}]$. The second loss function $L_{SLN-TF}$ is

$$L_{SLN-TF}(\boldsymbol{W}_{LRN}, \boldsymbol{b}_{LRN}) = \sqrt{\frac{1}{n}\left[\sum_{i=1}^{n}\left(x_i^{TF} - x_i\right)^2\right]} \quad (3)$$

where the parameters have the same meaning as those in (2). In addition, considering that the hidden layer states should be consistent in the FR and TF modes if there is no cumulative error, we define a third loss function $L_{SLN-PF}$ by the RMSE of the LSTM states between the two modes [professor forcing (PF)] [62]

$$L_{SLN-PF}(\boldsymbol{W}_{LRN}, \boldsymbol{b}_{LRN}) = \sqrt{\frac{1}{n}\left[\sum_{j=1}^{K}\sum_{i=0}^{n-1} h_i^{j'} - h_i^{j}\right]} \quad (4)$$

where $K$ is the number of the LSTM stacking layers ($K = 3$) and $h_i^{j}$ and $h_i^{j'}$ are the LSTM states at the $i$th time step of the $j$th layer in the FR and TF modes, respectively. Ultimately, the loss function $L_{SLN}$ of SLN is the sum of three loss functions

$$L_{SLN} = L_{SLN-FR} + L_{SLN-TF} + L_{SLN-PF}. \quad (5)$$

### D. Implementation

We use the Adam optimizer [63] to implement the RASE training. For UCN and SLN, the learning rates are $10^{-3}$ and $10^{-4}$ and the decay rates are $10^{-4}$ and $10^{-5}$, respectively. The open-source library Pytorch supports all the aforementioned
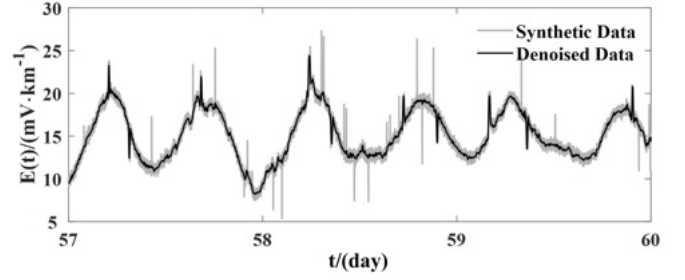


Fig. 3. Denoising result. Comparison between the synthetic data (gray) and denoising result (black) by the unsupervised convolution denoising network in the test set.
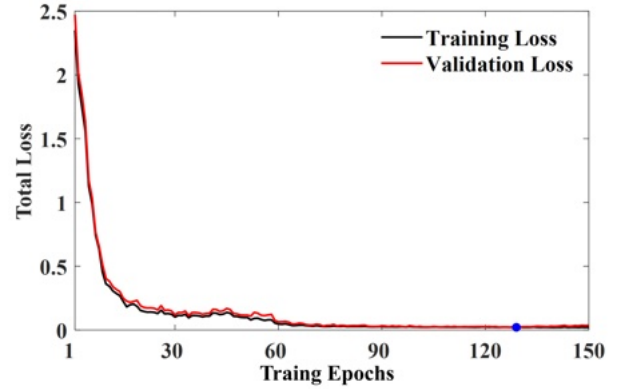


Fig. 4. Training of the supervised LSTM prediction network. Decrease of the loss functions of the training (black) and validation (red) sets with training epoch. One epoch indicates that the entire training and validation datasets are fed into the network to complete the calculation of the loss function and update the network parameters once. The blue solid dot indicates the location of the 128th epoch when the network achieves the best performance on the validation set.
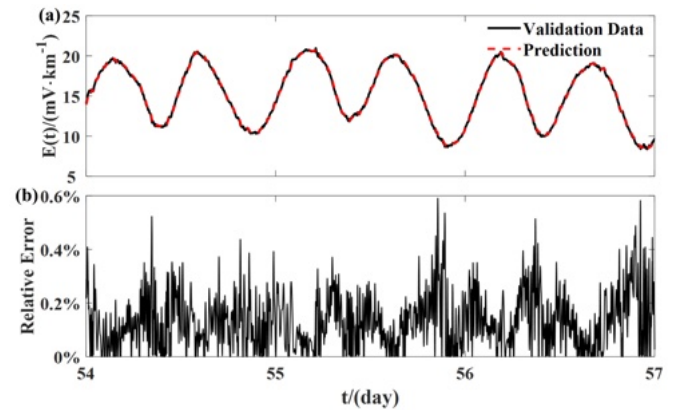


Fig. 5. Quality monitoring of the supervised LSTM prediction network. (a) Black solid and red dashed lines show the denoised data in the validation set and prediction result by the well-trained network, respectively. (b) Relative error between the denoised data and prediction result in (a).

deep learning concepts and optimization algorithms. All computations are carried out on a desktop personal computer (PC) equipped with an NVIDIA GeForce RTX 3070 GPU and an AMD Ryzen 7 3700X CPU with 16-GB memory. The RASE training takes about 2.73 and 2.42 h in the synthetic and field cases, respectively.
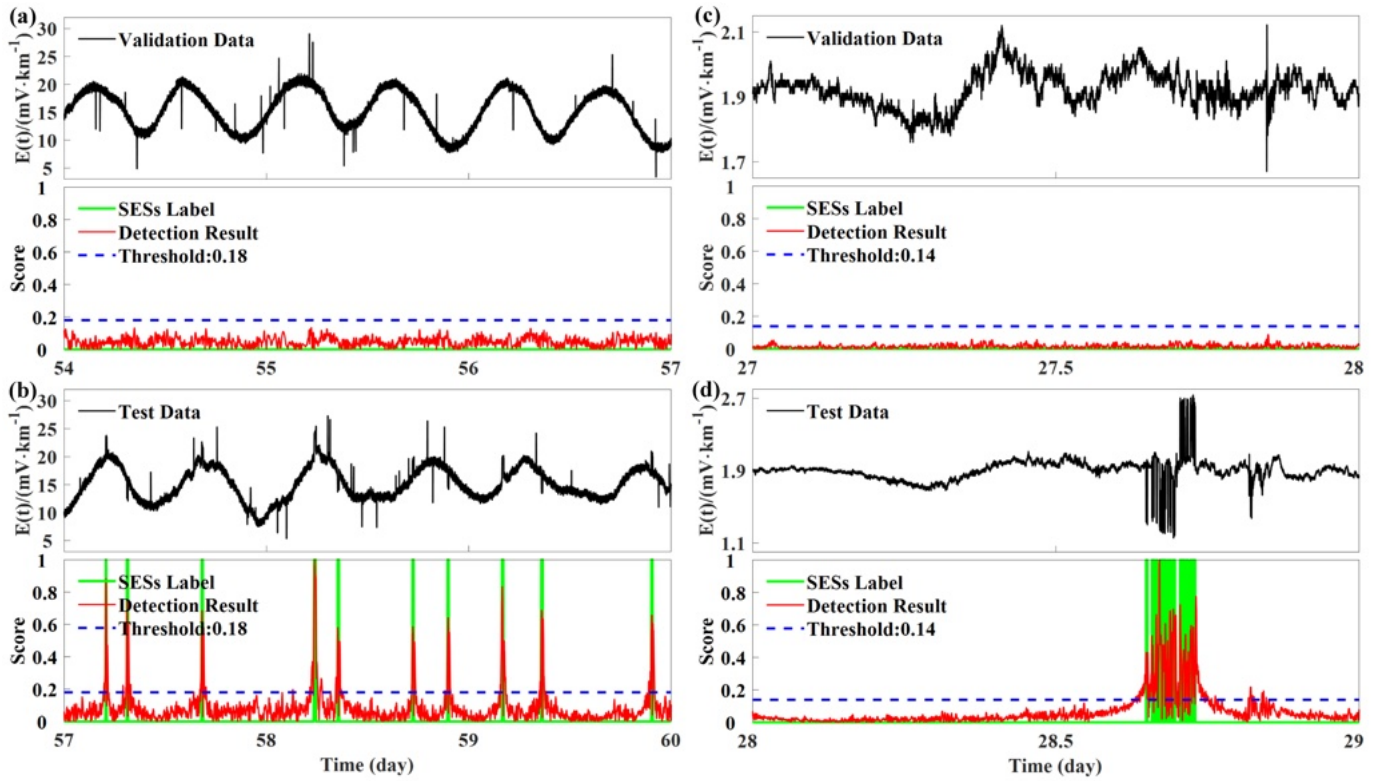
Fig. 6. Detection results using synthetic and field data. (a) Validation set for synthetic data. (b) Test set for synthetic data. (c) Validation set for field data. (d) Test set for field data. The black, green, red, and blue dotted lines show the original observations, manual binary labels of the SESs, detection results, and optimal thresholds determined by the ROC analysis, respectively.

## IV. RESULTS

### A. Synthetic Data

After the denoising process by UCN, the noise is successfully suppressed and the anomalous SESs are effectively retained (see Fig. 3). The denoised data are then used to train the downstream SLN of the RASE and the corresponding loss functions of both the training and test sets are monitored during the training process (see Fig. 4). The well-trained SLN is first examined by the validation dataset without anomalies. The prediction result shows good agreement with the denoised data with relative errors of less than 0.6% (see Fig. 5), indicating that the SLN is well-trained and has excellent prediction capability.

Fig. 6(a) and (b) shows the detection results of the RASE on the validation and test sets of the synthetic data. The detection result of the test set matches well with the manual binary labels. According to the ROC analysis of the test set [see Fig. 7(a)], when the optimal threshold (TH) is set to 0.18, the false positive rate (FPR) is 7.3%, the true positive rate (TPR) is 91.7%, and the area under the curve (AUC) reaches 0.963 (outstanding, see the Appendix for the classification criteria of AUC). Moreover, there are no false identification results on the validation set, as the anomaly score of each sampling point is always smaller than the selected threshold.

### B. Field Data

Fig. 6(c) and (d) shows the anomaly detection results for the validation and test sets of the field data. The ROC analysis

[see Fig. 7(b)] suggests that when the TH is 0.14, the FPR is 9.0%, the TPR is 95.7%, and the AUC reaches 0.975 (outstanding). The anomaly scores of the validation set are all well below the optimal threshold. In addition, the well-trained RASE takes only 31 s to complete anomaly detection for the 24-h continuous record, which can fully support the real-time detection requirement.

Results for both the synthetic and field data demonstrate that the RASE can accurately detect anomalous periods in real time and has the ability to fully extract effective information in a strong noise environment.

## V. DISCUSSION

### A. Length of the Training Set

Different lengths of the training set can often affect the detection accuracy. Unfortunately, to the best of our knowledge, there is no heuristic principle for choosing such a hyperparameter. Therefore, we examine the RASE's detection accuracy on the test set of the synthetic data by varying the lengths of the training set (see Fig. 8 and Table I).

The ROC curves largely overlap as the training set grows from 26 to 54 d, indicating that a significant increase in the training set length does not significantly improve the detection accuracy. However, an increase in the length of the training set will necessarily increase the training time. Therefore, we can choose the training set length to balance the training time and accuracy.
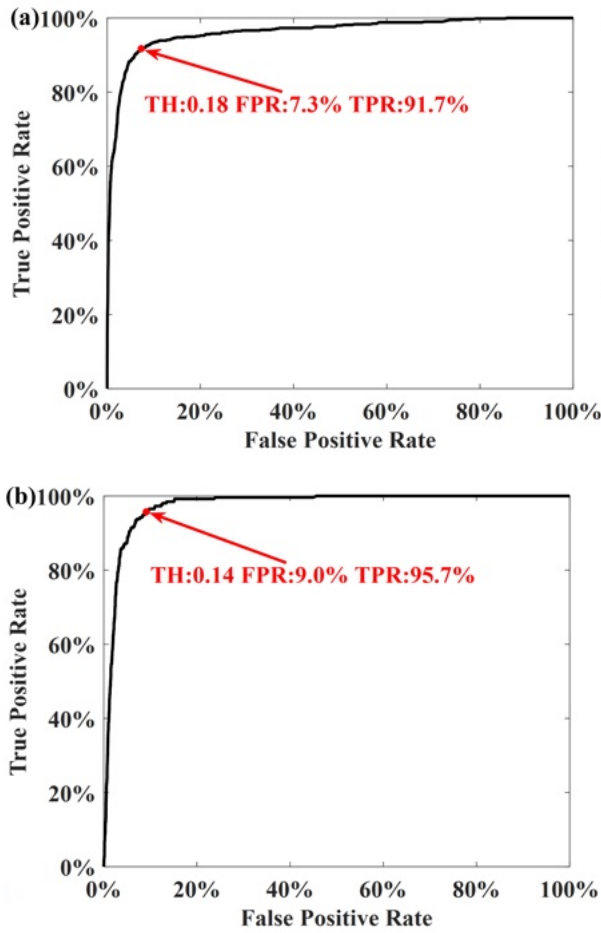
Fig. 7. ROC analyses of the anomaly detection results. (a) Synthetic data. (b) Field data. The red dots show the optimal operation points with threshold $S_T$ (=TH) selected based on the ROC analyses, representing that the RASE with the corresponding threshold achieves the best detection results on the test set.
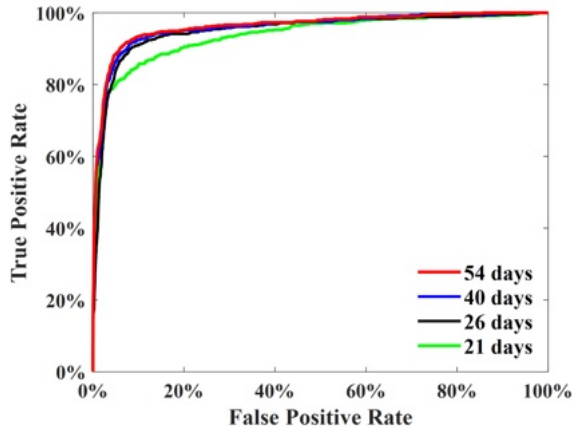


Fig. 8. Comparison of ROC analyses for different lengths of the training set. The red, blue, black, and green lines are the ROC curves of the RASE detection performances on the test set when the lengths of the training sets are 54, 40, 26, and 21 d, respectively.

With the training set length increasing from 21 to 26 d, the AUC grows from 0.938 to 0.951, indicating an "outstanding [AUC ∈ [0.95,1)]" detection performance according to the classification criteria of AUC in the Appendix. Therefore,
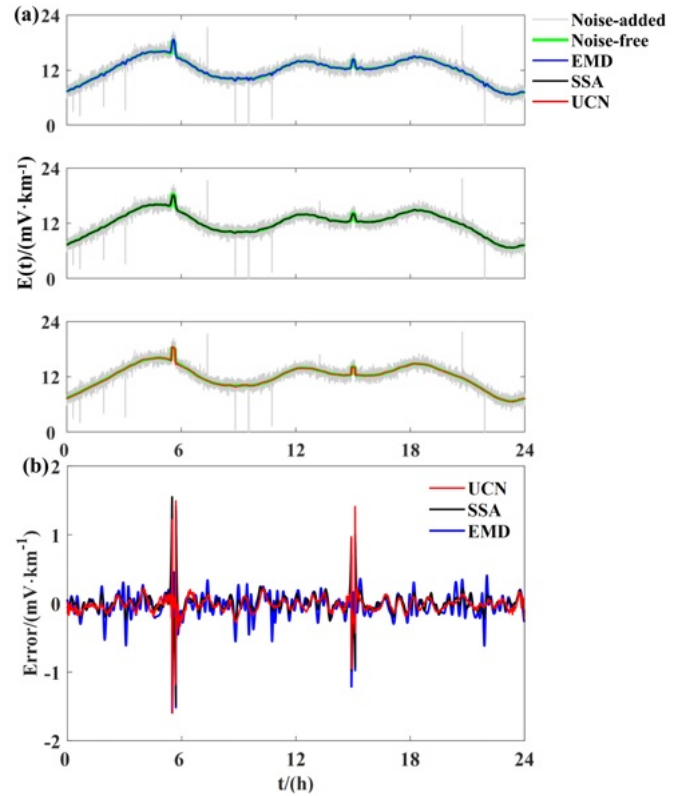


Fig. 9. Comparison of denoising performances of EMD, SSA, and UCN. (a) Denoising results of the three algorithms on the synthetic data. The gray, green, blue, black, and red lines indicate the noise-added data, noise-free data, and the EMD-, SSA-, and UCN-denoised results, respectively. (b) Error analyses of the denoising results by EMD (blue), SSA (black), and UCN (red). The errors are defined as the differences between the denoised and noise-free data, indicating the fidelities of the denoised signals. The quantitative results of the SNRs and errors of the three algorithms are listed in Table II.

TABLE I
EFFECT OF DIFFERENT LENGTHS OF THE TRAINING SET ON
DETECTION PERFORMANCE

| Duration | Fixed FPR | TPR | AUC | Training Time (h) |
|---|---|---|---|---|
| 54 Days | 7.3% | 91.7% | 0.963 | 2.73 |
| 40 Days | 7.3% | 89.7% | 0.959 | 2.56 |
| 26 Days | 7.3% | 88.3% | 0.951 | 2.31 |
| 21 Days | 7.3% | 84.1% | 0.938 | 2.27 |

we recommend choosing a training set length of 26 d to enable RASE to achieve "outstanding" detection performance with the lowest training cost.

## B. Comparison With Different Denoising Modules

The UCN algorithm has shown excellent denoising performance in seismic exploration [50], [51], [52]. However, for geoelectric field data, the UCN algorithm has not been compared with other conventional denoising algorithms. Here, we compare UCN with the EMD [45] and SSA [48] in terms of SNR and fidelity measures.

To facilitate the quantitative comparison of the denoising results, in this section, we incorporate in the first 54-d synthetic
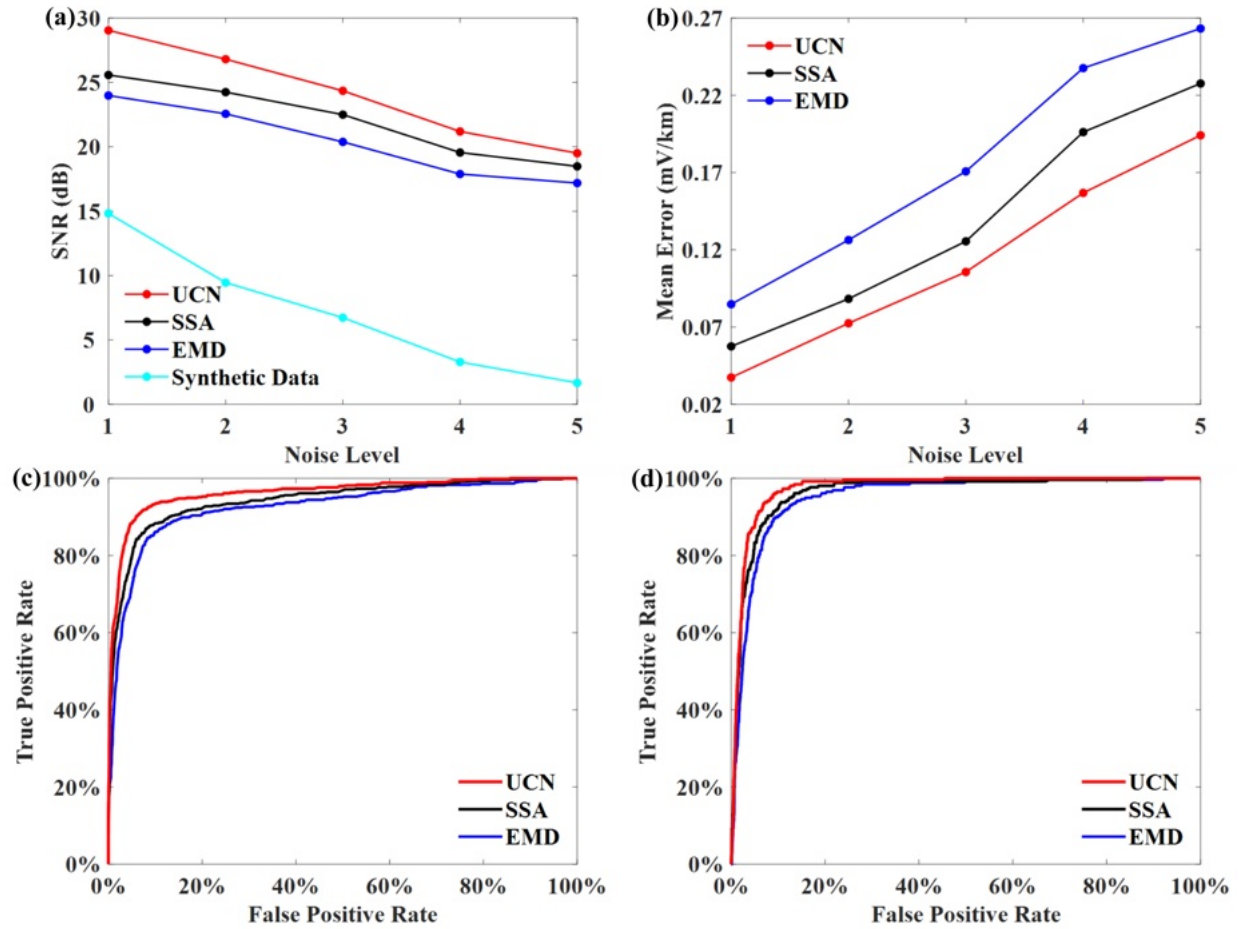
Fig. 10. Comparison of the UCN, SSA, and EMD denoising algorithms. (a) SNRs of the five noisy environments. (b) Fidelities in the five noisy environments. (c) and (d) ROC analyses of the three denoising algorithms on the synthetic and field data, respectively. The red, black, and blue lines represent the indicator values of denoising results [in (a) and (b)] and correlations between the true and FPRs [in (c) and (d)] obtained by the UCN, SSA, and EMD algorithms, respectively. The cyan line in (a) indicates the SNRs of the synthetic data contaminated by noises of the five different levels distributed between 0 and 15 dB.

data used the periodic tidal responses with anomalous SESs (considered as the noise-free data to be recovered), as well as interfering Gaussian and random impulsive noises [28]. We randomly select 1-d synthetic data for comparison and presentation. The denoising results [see Fig. 9(a)] and the corresponding errors [see Fig. 9(b)] suggest that the UCN algorithm achieves the best denoising performance with the highest fidelity for anomalous SESs among the three approaches. In addition, we calculate the average error at each sampling point to further compare the fidelity (see Table II). The quantitative comparison demonstrates that the UCN algorithm can obtain the best denoising effect with minimal signal impairment.

We also compare the robustness of the three denoising algorithms by adding into the synthetic data mixtures of Gaussian and random impulsive noises of five different levels of SNRs ranging between 0 and 15 dB. Fig. 10(a) and (b) shows the SNRs and fidelities, respectively, of the denoised signals using EMD, SSA, and UCN algorithms. Under various levels of noise interference, the UCN algorithm always achieves the greatest SNR and fidelity in the denoised signal compared to the other two conventional algorithms, demonstrating higher denoising robustness. In addition, the EMD and SSA require

fine parameter tuning for different noise levels to achieve the optimal denoising effect shown in Fig. 10(a) and (b), while the UCN needs less human intervention and is thus more suitable for practical scenarios with massive geoelectric field data.

In addition, we compare the impact of the EMD, SSA, and UCN denoising modules on the detection accuracy of the RASE. We use the same data and training strategy to ensure a fair comparison by the ROC analysis [see Fig. 10(c) and (d) and Tables III and IV]. Statistical results show that the UCN algorithm can significantly improve the RASE's detection performance compared to conventional denoising algorithms. Therefore, the RASE equipped with the UCN algorithm has the best detection robustness and stability, with the ROC analysis showing that its detection results are always outstanding (AUC > 0.95) in both synthetic and field cases.

### C. Comparison With Different Prediction Modules

In this section, we further investigate the impact of different prediction modules on the detection accuracy, aiming to find an optimal combination of modules that allows the RASE to achieve the best detection performance. We design a supervised recurrent neural network-based network (SRN),

TABLE II
COMPARISON OF SNR AND FIDELITIES OF EMD, SSA, AND UCN

| Denoising Method | SNR (dB) | Mean Error (mV/km) |
|---|---|---|
| UCN | 26.803 | 0.077 |
| SSA | 24.247 | 0.088 |
| EMD | 22.561 | 0.126 |

TABLE III
EFFECT OF DIFFERENT DENOISING MODULES ON THE DETECTION
PERFORMANCE OF THE SYNTHETIC DATA

| Denoising Method | Fixed FPR | TPR | AUC |
|---|---|---|---|
| UCN | 7.3% | 91.7% | 0.963 |
| SSA | 7.3% | 85.8% | 0.943 |
| EMD | 7.3% | 82.1% | 0.926 |

TABLE IV
EFFECT OF DIFFERENT DENOISING MODULES ON THE DETECTION
PERFORMANCE OF THE FIELD DATA

| Denoising Method | Fixed FPR | TPR | AUC |
|---|---|---|---|
| UCN | 9.0% | 95.7% | 0.975 |
| SSA | 9.0% | 91.5% | 0.964 |
| EMD | 9.0% | 89.5% | 0.952 |

TABLE V
EFFECT OF DIFFERENT PREDICTION MODULES ON THE DETECTION
PERFORMANCE OF THE SYNTHETIC DATA

| Prediction Method | Fixed FPR | TPR | AUC |
|---|---|---|---|
| SLN | 7.3% | 91.7% | 0.963 |
| SGN | 7.3% | 87.3% | 0.949 |
| SRN | 7.3% | 77.9% | 0.922 |

TABLE VI
EFFECT OF DIFFERENT PREDICTION MODULES ON THE DETECTION
PERFORMANCE OF THE FIELD DATA

| Prediction Method | Fixed FPR | TPR | AUC |
|---|---|---|---|
| SLN | 9.0% | 95.7% | 0.975 |
| SGN | 9.0% | 90.7% | 0.948 |
| SRN | 9.0% | 86.8% | 0.917 |

see [64], and a supervised gated recurrent unit-based network (SGN), see [65], and compare them with the current SLN in the RASE using the same UCN algorithm as the denoising module and the same data and training strategy.

Results of the synthetic and field data (see Fig. 11 and Tables V and VI) both suggest that the SLN-based RASE has the largest AUC, with TPR consistently higher than the other two algorithms, indicating that the RASE can provide the most accurate detection results. Combining the results of
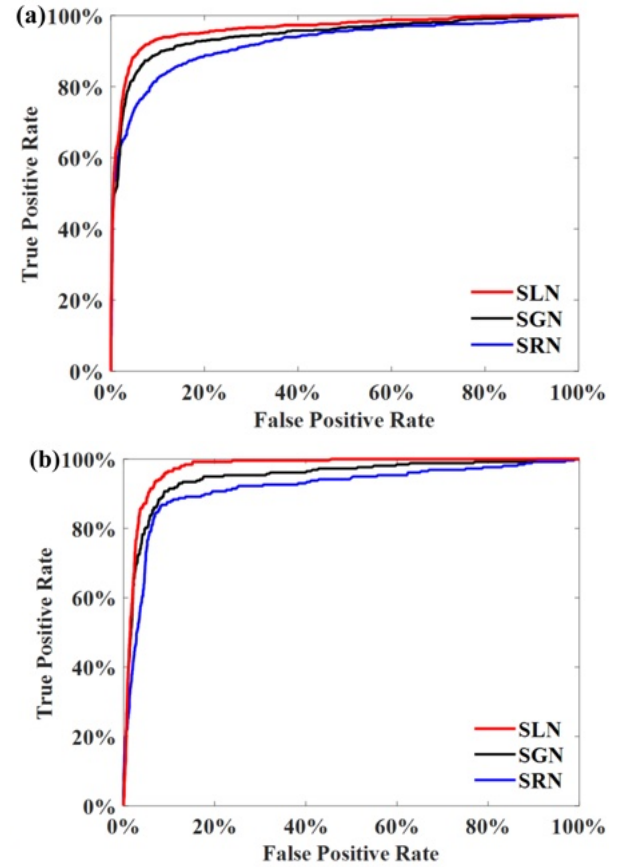


Fig. 11. Comparison of the three prediction modules. ROC analyses of the three prediction modules on (a) synthetic and (b) field data. The red, black, and blue lines represent the correlations between the true and FPRs obtained by the RASEs with prediction modules implemented by the three networks SLN, SGN, and SRN, respectively.

those in Figs. 10 and 11, the RASE based on the combination of UCN and SLN modules has the best detection accuracy in both synthetic and field data applications.

### D. Future Developments

In the RASE, the manually set threshold $S_T$ for the probability score defined in Section II-A is an important criterion for classifying anomalous SESs. A larger threshold value represents a more restrictive condition for identifying anomalies, leading to higher chances of missing anomalies but fewer false alarms. Therefore, the threshold should balance missed and false alarms so that they can be optimized simultaneously. According to the experimental results, the optimal threshold is generally between 0.1 and 0.2, which can be used as a reference for the subsequent threshold selection.

In addition, the denoising and prediction modules in the RASE can be easily adapted and reconstructed for different practical scenarios or replaced by better techniques. The current comparative experimental results demonstrate that our proposed RASE has excellent robustness and detection performance in noisy environments without elaborate parameter tuning. Moreover, the detection performance of the RASE can be further improved by incorporating better denoising and prediction modules developed in the future.

TABLE VII
CLASSIFICATION RESULTS OF THE ROC ANALYSIS

| | | Detection Results | |
|---|---|---|---|
| | | $S \geq S_T$ (1) | $S < S_T$ (0) |
| Artificial Labels | Anomaly (1) | TP | FN |
| | No Anomaly (0) | FP | TN |

Note: $S_T$ is a manually-set threshold in the ROC analysis, and $S$ is the anomaly score obtained by the RASE.

## VI. CONCLUSION

In this study, we have developed the RASE, a RASE for geoelectric field anomaly detection, which combines an unsupervised convolutional network for predenoising and a supervised LSTM prediction network for detecting anomalous SESs. Experiments using the synthetic and real anomalous SESs demonstrate that the RASE provides excellent detection accuracy and efficiency. Comparison with several denoising and prediction algorithms shows that the UCN algorithm has the best denoising robustness without elaborate parameter tuning, and the combination of UCN and SLN delivers optimal detection performance. Our proposed RASE can support the need for real-time automatic anomaly search in massive geoelectric field data in the future.

## APPENDIX

We use the ROC analysis [53], [54] to quantitatively evaluate the detection performance of the RASE. The binary representation of the SESs is a two-value time series: 1 indicates an anomaly when the SES exists at time $t$, whereas 0 indicates no anomaly [12], [24]. According to the RASE's detection result, the time is marked as 1 if the detection score $S$ is greater than a manually set threshold value $S_T$ or 0 otherwise.

We use the ROC analysis to compare the RASE's detection results with manual SES labels and classify the detection results into four categories (see Table VII): true positive (TP), false negative (FN), false positive (FP), and true negative (TN). The TPR and FPR are calculated based on the aforementioned classification results

$$\text{TPR} = \frac{\text{TP}}{\text{TP+FN}} \tag{A-1}$$

$$\text{FPR} = \frac{\text{FP}}{\text{FP+TN}}. \tag{A-2}$$

The ROC curve illustrates the relationship between the FPR ($x$-axis) and TPR ($y$-axis), and the area under the ROC curve quantifies the detection accuracy. In this study, referring to the classification criteria of Sarlis et al. [66], we classify the performance of the RASE by the AUC as: "invalid" [AUC $\in$ [0, 0.5)], "poor" [AUC $\in$ [0.5–0.7)], "acceptable" [AUC $\in$ [0.7–0.8)], "excellent" [AUC $\in$ [0.8–0.95)], "outstanding" [AUC $\in$ [0.95, 1)], and "perfect" (AUC = 1). According to the ROC curve, we can determine the optimal threshold that maximizes the difference between the TPR and FPR. In addition, the FPR focuses only on the anomalous samples, while the TPR focuses only on the no anomaly samples so that the ROC is suitable for geoelectric field data even with an unbalanced proportion of positive and negative samples.

## REFERENCES

[1] S. Uyeda, T. Nagao, and M. Kamogawa, "Short-term earthquake prediction: Current status of seismo-electromagnetics," *Tectonophysics*, vol. 470, nos. 3–4, pp. 205–213, May 2009.

[2] Q. Huang and T. Nagao, "Seismic quiescence before the 2000 M = 7.3 Tottori earthquake," *Geophys. Res. Lett.*, vol. 29, no. 12, p. 1578, 2002.

[3] G. A. Sobolev, Q. Huang, and T. Nagao, "Phases of earthquake's preparation and by chance test of seismic quiescence anomaly," *J. Geodyn.*, vol. 33, nos. 4–5, pp. 413–424, May 2002.

[4] P. Varotsos, N. V. Sarlis, and E. S. Skordas, *Natural Time Analysis: The New View of Time: Precursory Seismic Electric Signals, Earthquakes and Other Complex Time Series*. Berlin, Germany: Springer-Verlag, 2011.

[5] Q. Huang and X. Ding, "Spatiotemporal variations of seismic quiescence prior to the 2011 M 9.0 Tohoku earthquake revealed by an improved region–time–length algorithm," *Bull. Seismol. Soc. Amer.*, vol. 102, no. 4, pp. 1878–1883, 2012.

[6] K. F. Tiampo and R. Shcherbakov, "Seismicity-based earthquake forecasting techniques: Ten years of progress," *Tectonophysics*, vols. 522–523, pp. 89–121, Feb. 2012.

[7] N. V. Sarlis et al., "Minimum of the order parameter fluctuations of seismicity before major earthquakes in Japan," *Proc. Nat. Acad. Sci. USA*, vol. 110, no. 34, pp. 13734–13738, 2013.

[8] P. Varotsos and K. Alexopoulos, "Physical properties of the variations of the electric field of the Earth preceding earthquakes, I," *Tectonophysics*, vol. 110, nos. 1–2, pp. 73–98, Dec. 1984.

[9] P. Varotsos and K. Alexopoulos, "Physical properties of the variations of the electric field of the Earth preceding earthquakes. II. Determination of epicenter and magnitude," *Tectonophysics*, vol. 110, nos. 1–2, pp. 99–125, 1984.

[10] S. Uyeda, T. Nagao, Y. Orihara, T. Yamaguchi, and I. Takahashi, "Geoelectric potential changes: Possible precursors to earthquakes in Japan," *Proc. Nat. Acad. Sci. USA*, vol. 97, no. 9, pp. 4561–4566, Apr. 2000.

[11] Q. Huang, H. Ren, D. Zhang, and Y. J. Chen, "Medium effect on the characteristics of the coupled seismic and electromagnetic signals," *Proc. Jpn. Acad., B*, vol. 91, no. 1, pp. 17–24, 2015.

[12] P. Varotsos, N. Sarlis, and E. Skordas, "Electric fields that 'arrive' before the time derivative of the magnetic field prior to major earthquakes," *Phys. Rev. Lett.*, vol. 91, no. 14, 2003, Art. no. 148501.

[13] K. Hattori, "ULF geomagnetic changes associated with large earthquakes," *Terr., Atmos. Ocean. Sci.*, vol. 15, no. 3, pp. 329–360, 2004.

[14] G. Xu, P. Han, Q. Huang, K. Hattori, F. Febriani, and H. Yamaguchi, "Anomalous behaviors of geomagnetic diurnal variations prior to the 2011 off the Pacific coast of Tohoku earthquake (Mw9.0)," *J. Asian Earth Sci.*, vol. 77, pp. 59–65, Nov. 2013.

[15] P. A. Varotsos, *The Physics of Seismic Electric Signals*. Tokyo, Japan: TerraPub, 2005.

[16] G. Zhao et al., "A review of seismo-electromagnetic research in China," *Sci. China Earth Sci.*, vol. 65, no. 7, pp. 1229–1246, 2022.

[17] Q. Huang and Y. Lin, "Selectivity of seismic electric signal (SES) of the 2000 Izu earthquake swarm: A 3D FEM numerical simulation model," *Proc. Jpn. Acad., B*, vol. 86, no. 3, pp. 257–264, 2010.

[18] H. Ren, X. Chen, and Q. Huang, "Numerical simulation of coseismic electromagnetic fields associated with seismic waves due to finite faulting in porous media," *Geophys. J. Int.*, vol. 188, no. 3, pp. 925–944, Mar. 2012.

[19] N. V. Sarlis, "Statistical significance of Earth's electric and magnetic field variations preceding earthquakes in Greece and Japan revisited," *Entropy*, vol. 20, no. 8, p. 561, 2018.

[20] F. Jiang, X. Chen, C.-C. Chen, and H.-J. Chen, "Relationship between seismic electric signals and tectonics derived from dense geoelectric observations in Taiwan," *Pure Appl. Geophys.*, vol. 177, no. 1, pp. 441–454, Jan. 2020.

[21] P. A. Varotsos, N. V. Sarlis, and E. S. Skordas, "Phenomena preceding major earthquakes interconnected through a physical model," *Annales Geophysicae*, vol. 37, no. 3, pp. 315–324, May 2019.

[22] P. Varotsos, N. Sarlis, and E. Skordas, "Order parameter and entropy of seismicity in natural time before major earthquakes: Recent results," *Geosciences*, vol. 12, no. 6, p. 225, May 2022.

[23] P. Varotsos and M. Lazaridou, "Latest aspects of earthquake prediction in Greece based on seismic electric signals," *Tectonophysics*, vol. 188, nos. 3–4, pp. 321–347, Mar. 1991.

[24] P. A. Varotsos, N. V. Sarlis, and E. S. Skordas, "Long-range correlations in the electric signals that precede rupture," *Phys. Rev. E, Stat. Phys. Plasmas Fluids Relat. Interdiscip. Top.*, vol. 66, no. 1, Jul. 2002, Art. no. 011902.

[25] P. A. Varotsos, N. V. Sarlis, and E. S. Skordas, "Attempt to distinguish electric signals of a dichotomous nature," *Phys. Rev. E, Stat. Phys. Plasmas Fluids Relat. Interdiscip. Top.*, vol. 68, no. 3, Sep. 2003, Art. no. 031106.

[26] Z. An, X. Du, D. Tan, Y. Fan, J. Liu, and T. Cui, "Study on the geo-electric field variation of Sichuan Lushan $M_S$7.0 and Wenchuan $M_S$8.0 earthquake," *Chin. J. Geophys.*, vol. 56, no. 6, pp. 721–730, 2013.

[27] J. Xi et al., "Dynamic changes of second sampling geoelectric field observation data before and after Qinghai Madoi Ms7.4 earthquake," *Chin. J. Geophys.*, vol. 65, no. 2, pp. 580–593, 2022.

[28] K. Wang, Q. Huang, and S. Wu, "Application of long short-term memory neural network in geoelectric field data processing," *Chin. J. Geophys.*, vol. 63, no. 8, pp. 3015–3024, 2020.

[29] J. Xue, Q. Huang, S. Wu, and T. Nagao, "LSTM-autoencoder network for the detection of seismic electric signals," *IEEE Trans. Geosci. Remote Sens.*, vol. 60, 2022, Art. no. 5917012.

[30] Y. LeCun, Y. Bengio, and G. Hinton, "Deep learning," *Nature*, vol. 521, no. 7553, pp. 436–444, 2015.

[31] D. Kwon, H. Kim, J. Kim, S. C. Suh, I. Kim, and K. J. Kim, "A survey of deep learning-based network anomaly detection," *Cluster Comput.*, vol. 22, pp. 949–961, Sep. 2017.

[32] S. Chauhan and L. Vig, "Anomaly detection in ECG time signals via deep long short-term memory networks," in *Proc. IEEE Int. Conf. Data Sci. Adv. Analytics (DSAA)*, Pairs, France, Oct. 2015, pp. 1–7.

[33] S. Ahmad, A. Lavin, S. Purdy, and Z. Agha, "Unsupervised real-time anomaly detection for streaming data," *Neurocomputing*, vol. 262, pp. 134–147, Nov. 2017.

[34] L. Basora, X. Olive, and T. Dubot, "Recent advances in anomaly detection methods applied to aviation," *Aerospace*, vol. 6, no. 11, p. 117, Oct. 2019.

[35] R. Chalapathy and S. Chawla, "Deep learning for anomaly detection: A survey," 2019, *arXiv:1901.03407*.

[36] S. Eyuboglu et al., "Multi-task weak supervision enables anatomically-resolved abnormality detection in whole-body FDG-PET/CT," *Nature Commun.*, vol. 12, no. 1, p. 1880, 2021.

[37] T. Oktay, E. Yoğurtçuoğlu, R. N. Sarikaya, A. R. Karaca, M. F. Kömürcü, and A. Sayar, "Multimodel anomaly detection on spatio-temporal logistic datastream with open anomaly detection architecture," *Expert Syst. Appl.*, vol. 186, Dec. 2021, Art. no. 115755.

[38] S. Kanarachos, S.-R. G. Christopoulos, A. Chroneos, and M. E. Fitzpatrick, "Detecting anomalies in time series data via a deep learning algorithm combining wavelets, neural networks and Hilbert transform," *Expert Syst. Appl.*, vol. 85, pp. 292–304, Nov. 2017.

[39] Q.-H. Huang and T. Liu, "Earthquakes and tide response of geoelectric potential field at the Niijima station," *Chin. J. Geophys.*, vol. 49, no. 6, pp. 1585–1594, Nov. 2006.

[40] S. Hochreiter and J. Schmidhuber, "Long short-term memory," *Neural Comput.*, vol. 9, no. 8, pp. 1735–1780, 1997.

[41] F. A. Gers, J. Schmidhuber, and F. Cummins, "Learning to forget: Continual prediction with LSTM," *Neural Comput.*, vol. 12, no. 10, pp. 2451–2471, 2000.

[42] S. Wu, Q. Huang, and L. Zhao, "De-noising of transient electromagnetic data based on the long short-term memory-autoencoder," *Geophys. J. Int.*, vol. 224, no. 1, pp. 669–681, Nov. 2020.

[43] S. Wu, Q. Huang, and L. Zhao, "Instantaneous inversion of airborne electromagnetic data based on deep learning," *Geophys. Res. Lett.*, vol. 49, no. 10, May 2022, Art. no. e2021GL097165.

[44] S. Wold, K. Esbensen, and P. Geladi, "Principal component analysis," *Chemometrics Intell. Lab. Syst.*, vol. 2, nos. 1–3, pp. 37–52, 1987.

[45] N. E. Huang et al., "The empirical mode decomposition and the Hilbert spectrum for nonlinear and non-stationary time series analysis," *Proc. Roy. Soc. London A, Math., Phys. Eng. Sci.*, vol. 454, no. 1971, pp. 903–995, 1998.

[46] L. Telesca, G. Colangelo, K. Hattori, and V. Lapenna, "Principal component analysis of geoelectrical signals measured in the seismically active area of Basilicata region (southern Italy)," *Natural Hazards Earth Syst. Sci.*, vol. 4, no. 5/6, pp. 663–667, Nov. 2004.

[47] S. G. Chang, B. Yu, and M. Vetterli, "Adaptive wavelet thresholding for image denoising and compression," *IEEE Trans. Image Process.*, vol. 9, no. 9, pp. 1532–1546, Sep. 2000.

[48] R. Vautard, P. Yiou, and M. Ghil, "Singular-spectrum analysis: A toolkit for short, noisy chaotic signals," *Phys. D, Nonlinear Phenomena*, vol. 58, pp. 95–126, Sep. 1992.

[49] S. Saito, D. Kaida, K. Hattori, F. Febriani, and C. Yoshino, "Signal discrimination of ULF electromagnetic data with using singular spectrum analysis—An attempt to detect train noise," *Natural Hazards Earth Syst. Sci.*, vol. 11, no. 7, pp. 1863–1874, 2011.

[50] M. Zhang, Y. Liu, M. Bai, and Y. Chen, "Seismic noise attenuation using unsupervised sparse feature learning," *IEEE Trans. Geosci. Remote Sens.*, vol. 57, no. 12, pp. 9709–9723, Dec. 2019.

[51] O. M. Saad and Y. Chen, "Deep denoising autoencoder for seismic random noise attenuation," *Geophysics*, vol. 85, no. 4, pp. V367–V376, Jul. 2020.

[52] B. Liu et al., "Unsupervised deep learning for random noise attenuation of seismic data," *IEEE Geosci. Remote Sens. Lett.*, vol. 19, pp. 1–5, 2021.

[53] T. Fawcett, "An introduction to ROC analysis," *Pattern Recognit. Lett.*, vol. 27, no. 8, pp. 861–874, Jun. 2005.

[54] S.-R.-G. Christopoulos, G. I. Tsagiannis, K. A. Papadopoulou, and N. V. Sarlis, "VISROC 2.0: Updated software for the visualization of the significance of receiver operating characteristics based on confidence ellipses," *Comput. Phys. Commun.*, vol. 280, Nov. 2022, Art. no. 108492.

[55] Y. Orihara, M. Kamogawa, T. Nagao, and S. Uyeda, "Independent component analysis of geoelectric field data in the northern Nagano, Japan," *Proc. Jpn. Acad., B*, vol. 85, no. 9, pp. 435–442, 2009.

[56] P. Varotsos, N. Sarlis, and E. Skodras, "A note on the spatial extent of the Volos SES sensitive site," *Acta Geophys. Polonica*, vol. 49, no. 4, pp. 425–435, 2001.

[57] Y. Chen, M. Zhang, M. Bai, and W. Chen, "Improving the signal-to-noise ratio of seismological datasets by unsupervised machine learning," *Seismol. Res. Lett.*, vol. 90, no. 4, pp. 1552–1564, 2019.

[58] D. E. Rumelhart, G. E. Hinton, and R. J. Williams, "Learning representations by back-propagating errors," *Nature*, vol. 323, no. 6088, pp. 533–536, Oct. 1986.

[59] S. Ioffe and C. Szegedy, "Batch normalization: Accelerating deep network training by reducing internal covariate shift," in *Proc. 32nd Int. Conf. Mach. Learn. (ICML)*, Lile, France, 2015, pp. 448–456.

[60] R. J. Williams and D. Zipser, "A learning algorithm for continually running fully recurrent neural networks," *Neural Comput.*, vol. 1, no. 2, pp. 270–280, 1989.

[61] I. Goodfellow, Y. Bengio, and A. Courville, *Deep Learning*. Cambridge, MA, USA: MIT Press, 2016.

[62] A. Lamb, A. Goyal, Y. Zhang, S. Zhang, A. Courville, and Y. Bengio, "Professor forcing: A new algorithm for training recurrent networks," 2016, *arXiv:1610.09038*.

[63] D. P. Kingma and J. Ba, "Adam: A method for stochastic optimization," 2014, *arXiv:1412.6980*.

[64] K. Cho et al., "Learning phrase representations using RNN encoder–decoder for statistical machine translation," 2014, *arXiv:1406.1078*.

[65] J. Chung, C. Gulcehre, K. Cho, and Y. Bengio, "Empirical evaluation of gated recurrent neural networks on sequence modeling," 2014, *arXiv:1412.3555*.

[66] N. V. Sarlis, E. S. Skordas, S.-R.-G. Christopoulos, and P. A. Varotsos, "Natural time analysis: The area under the receiver operating characteristic curve of the order parameter fluctuations minima preceding major earthquakes," *Entropy*, vol. 22, no. 5, p. 583, May 2020.
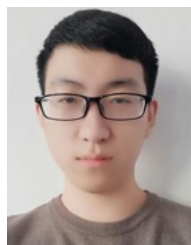
**Jiyan Xue** received the B.S. degree in geophysics from the China University of Geosciences, Wuhan, China, in 2020. He is currently pursuing the Ph.D. degree with the Department of Geophysics, Peking University, Beijing, China, under the supervision of Prof. Q. Huang.

His research interests include electromagnetic data processing, radar signal inversion, and deep learning.

**Sihong Wu** received the B.S. degree in geophysics from the University of Science and Technology of China, Hefei, Anhui, China, in 2016, and the Ph.D. degree in solid geophysics from Peking University, Beijing, China, in 2021.

She is currently a Post-Doctoral Fellow with the Department of Geophysics, Peking University. Her research interests include airborne electromagnetic data processing, forward modeling and inversion, and deep learning.

**Nicholas V. Sarlis** received the Ph.D. degree in solid-state physics from the National and Kapodistrian University of Athens (NKUA), Zografou, Greece, in 1997.

He is currently a Professor with the Department of Physics, NKUA. He has authored one monograph and more than 155 peer-reviewed scientific publications. His research interests include solid-state physics, propagation of electromagnetic signals in inhomogeneous media, physics of Earth's solid crust, and physics of complex systems with applications in seismology and heart dynamics.

**Qinghua Huang** received the Ph.D. degree in physics from Osaka University, Osaka, Japan, in 1999.

He is currently a Professor of geophysics with Peking University, Beijing, China. He has coauthored more than 120 articles in national and international journals. His research interests include the development of new algorithms, methodologies, and models for geoscience applications.

Prof. Huang was a recipient of the First Prize for Science and Technology of Chinese Geophysics by the Chinese Geophysical Society (CGS) in 2016. He is the Vice-President of the Seismological Society of China, the Vice-President of the Chinese Geophysical Society, the Deputy Editor-in-Chief of *Chinese Journal of Geophysics*, and an Associate Editor of the *Journal of Geophysical Research: Solid Earth*.

**Li Zhao** received the Ph.D. degree in geophysics from Princeton University, Princeton, NJ, USA, in 1995.

He is currently a Chair Professor with Peking University, Beijing, China, where he also serves as the Director of the Institute of Theoretical and Applied Geophysics, School of Earth and Space Sciences. He has published more than 100 articles in professional journals. His research focuses on the development and application of full-waveform seismic tomography.

Dr. Zhao is an Associate Editor of the *Journal of Geophysical Research: Solid Earth*.
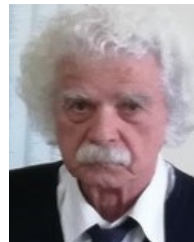
**Panayiotis A. Varotsos** received the Ph.D. degree in physics from the National and Kapodistrian University of Athens (NKUA), Zografou, Greece, in 1973.

He is currently a Professor with the Department of Physics, NKUA. He has authored five books and more than 250 articles in refereed scientific journals. His research interests include solid-state physics, statistical physics (critical phenomena), physics of complex systems (natural time analysis), and geophysics (preseismic variations of the electric and magnetic field of the Earth).

Dr. Varotsos received the Prize of the Academy of Athens in 1978, the Prize of the "Empirikion" Foundation in 1986, and the "A. S. Onassis" Foundation Laureate for the Environment in 1995. He has invented the so-called VAN method of short-term earthquake prediction.